PAPER

Transient buildup and dissipation of a compressed plasma shockwave in arc-discharge plasma beams

To cite this article: Zhe Zhang *et al* 2021 *Plasma Sources Sci. Technol.* **30** 125014

IOP Publishing Plasma Sources Science and Technology
Plasma Sources Sci. Technol. **30** (2021) 125014 (15pp) https://doi.org/10.1088/1361-6595/ac3bd5

Transient buildup and dissipation of a compressed plasma shockwave in arc-discharge plasma beams

Zhe Zhang[1,2], Yifeng Fu[3], Zun Zhang[3], Xin Lin[4], Jiayun Qi[3], William Yeong Liang Ling[5], Haibin Tang[6,7,8,*] and Georg Herdrich[2]

[1] School of Instrumentation and Optoelectronic Engineering, Beihang University, Beijing 100191, People's Republic of China
[2] University of Stuttgart, Institute of Space Systems, 70569 Stuttgart, Germany
[3] School of Space and Environment, Beihang University, Beijing 100191, People's Republic of China
[4] Institute of Mechanics, Chinese Academy of Sciences, Beijing 100080, People's Republic of China
[5] School of Aerospace Engineering, Beijing Institute of Technology, Beijing 100081, People's Republic of China
[6] School of Astronautics, Beihang University, Beijing, 100191, People's Republic of China
[7] Key Laboratory of Spacecraft Design Optimization and Dynamic Simulation Technologies, Ministry of Education, Beijing, 102206, Beijing, People's Republic of China
[8] Laboratory of Space Environment Monitoring and Information Processing, Ministry of Industry and Information Technology, Beijing, 102206, Beijing, People's Republic of China

E-mail: thb@buaa.edu.cn

Received 13 October 2021
Accepted for publication 22 November 2021
Published 23 December 2021

Abstract

Electric propulsion offers the advantage of a high specific impulse through a large exhaust velocity and has seen significant progress in space flight applications. Recently, we observed a transient plasma shockwave during pulsed plasma thruster operation when the plasma beam impacted a probe surface. However, details regarding the plasma shockwave formation are still unknown. This work is an experimental investigation of the compression-induced plasma shockwave in the presence of a planar obstruction. To study the complete shockwave buildup and dissipation process, an ultra-high-speed imaging system was set up to visualize the time-resolved shockwave morphology at a sub-microsecond level. In addition, the local magnetic field and plasma density were measured using 2D magnetic coils and a triple Langmuir probe, respectively. The successive images of the shockwave give us a comprehensive understanding of the shockwave buildup process. During the 12 μs operational period of the thruster, two shockwaves were formed during the first cycle of the discharge. It is also interesting to note that there is a 1 μs dissipation period between the two shockwaves with the same cloud of plasma compressing against the probe surface. A shockwave model is also developed to predict the appearance of the two shockwaves. The implication is that the local magnetic field strength can be a key indicator for the plasma shockwave buildup and dissipation process.

Keywords: electric propulsion, plasma shockwave, ultra-high speed imaging, plasma compression

(Some figures may appear in colour only in the online journal)

* Author to whom any correspondence should be addressed.

1. Introduction

Electric propulsion (EP) systems are plasma sources with the advantage of a high fuel efficiency, making them popular for spacecraft orbital control [1]. They are able to generate low temperature plasma populations such as Xe^+, Ar^+, C^+, and F^+. Under an appropriate electromagnetic field, ions can be accelerated to an exhaust velocity of 10 to 50 km s^{-1}. This produces a plasma plume with high directionality and velocity [2]. Although the early adoption of EP technology was mainly focused on space applications, nowadays, people have begun to look into physical processes such as ionization, arc discharges, electromagnetic acceleration, and plasma propagation to improve the performance of EP systems [3]. Recently, we observed that a plasma bowshock formed in front of a planar probe in the plasma beam of our EP thruster. However, many of the buildup mechanisms and plasma processes behind this phenomenon still remain unknown. This plasma shockwave phenomenon not only allows us to re-examine the influence of shockwaves on EP devices, but also leads to further consideration and thought regarding the fundamental build-up and dissipation processes of shockwaves in low-temperature plasmas.

Objects blocking high-speed plasma beams will cause plasma compression, followed by the formation and the dissipation of shockwave disturbances [4, 5]. Such processes involving the nature of the plasma shockwave are widely applicable in various fields such as atmospheric reentry [6, 7], plasma diagnostic [8], target measurement [9], and fusion [10].

Usually, small disturbances in the plasma beam are propagated as ion acoustic waves [11, 12] when the supersonic plasma is momentarily blocked by a flat object (a discontinuous surface), resulting in the formation of a shockwave. At the same time, with compression and heating, the corresponding plasma density, velocity, and temperature are discontinuous. Research on shockwaves in fluid mechanics has been relatively clear on some levels [13], however, the establishment of plasma shockwaves and the mechanism behind the buildup instability and dissipation process still remain unclear due to the complex magnetohydrodynamics (MHDs). The plasma shockwave plays a dual role in understanding the process of a magnetic fluid being compressed: (i) it reveals the compression conditions and duration of a plasma shock, which are important in the formation of ultra-high-density plasmas; (ii) the magnetic field compression accompanying plasma compression is a feature that a neutral fluid shockwave does not possess.

In past works, fluid methods [14], particle-in-cell methods [15], and hybrid kinetic methods [16] have been used to establish simulation models for plasma shockwaves. The target research objects of these models are mainly stationary and quasi-stationary shockwaves, whereas hot and dilute space plasma exist in the Universe [17]. On the other hand, most experimental plasma shockwaves are generated by laser ablation [18, 19]. With the fast development of EP, increasing efforts have been devoted to optimizing the plasma beam density and plasma exhaust velocity [20]. This has led to optimizations in high current density in plasma jets [21], and in high acceleration in EP plasma beams [22]. This is the reason that we can observe some weak shockwaves in the plasma beams of EP thrusters. It has been reported that a plasma bowshock is formed in front of a probe during the ignition of a pulsed plasma thruster (PPT) [23]. PPTs are typical EP thrusters that operate in a vacuum environment. They discharge within an extremely short time, and undergo ionization and ablation during a single pulse. In the presence of the strong 20 kA level discharge current, highly ionized plasma is accelerated by an induced magnetic field [24, 25]. This indicates that the formation of the shockwave is a sub-microsecond transient process that appears in arc-discharge plasma beams under an electromagnetic field environment. The shockwave in a PPT beam can be viewed from a magnetic fluid mechanics point of view, and is not widely concerning in the area of EP. No further investigations exist so far beyond the long-exposure images of a plasma shockwave outlined here. A number of fundamental questions regarding the shockwave formation conditions, duration, configurations, and dissipation process require further study.

Instead of specific PPT performance studies such as those performed in the past few decades [26], experiments have been conducted here to measure the buildup and dissipation process to study the physical process of the shockwave buildup. In addition, reasonable agreement has been obtained with proposed models. In contrast with a traditional fluid shockwave, the plasma shockwave observed in this work needs to consider the induced electromagnetic field and plasma propagation characteristics. This work aims to achieve an in-depth understanding of the buildup and dissipation process of the plasma shock from an experimental point of view. Ultimately, through experiments and theoretical analysis, we believe this work can introduce new insights into plasma shockwave measurements and the associated physical process across the low temperature plasma research area. Regarding the plasma shockwave measurement aspect, instead of measuring the temperature, configuration, scattered light, and pressure outside the shockwave [27], we inserted a 2D magnetic coil inside a planar obstruction to obtain the local magnetic field variations near the shockwave. A Langmuir probe is also used to measure the ion density around the shock formation area. Additionally, an ultra-high-speed camera is used to obtain a complete visualization of the plasma shockwave buildup and dissipation process. This will unravel the effects of the plasma density, block distance, and magnetic field strength on plasma shockwaves on a sub-microsecond level. These experiments demonstrate the magnetic fluid nature of compressed plasma beams. Furthermore, to gain a more general understanding of the shockwave in PPTs, a MHD model is also developed to describe the buildup, duration, and dissipation process.

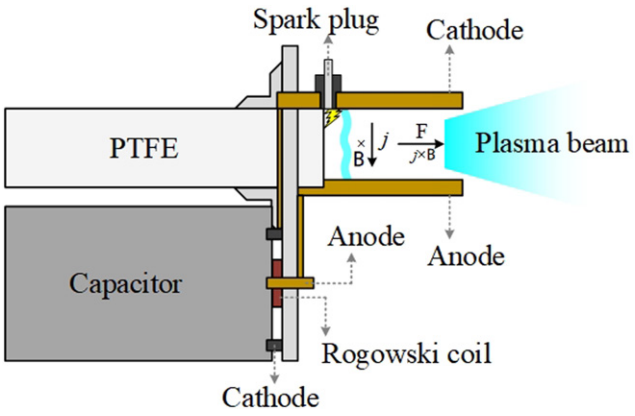

Figure 1. A schematic of the experimental PPT.

2. Experimental apparatus

2.1. Pulsed plasma shockwave generation system

Experiments were performed using a parallel-plate ablative PPT. A schematic of the PPT is shown in figure 1. The discharge channel of the PPT is a cuboid volume with an inner height of 28 mm, comprised of two copper parallel electrodes of 15 mm in length. The propellant used here is the polymer polytetrafluoroethylene (PTFE). The ablation and ionization of plasma was driven by a 1000 to 2000 V voltage differential applied to the electrodes, while the cathode and the chamber walls were grounded. An energy storage device (an oil capacitor) is used here to store the discharge energy required for every discharge (shot) from the PPT. A Rogowski coil is used here to measure the discharge current.

For a single shot of the PPT, a spark plug initially generates some electrons near the cathode, and an electron avalanche develops between the cathode and anode along the PTFE surface. A discharge arc is then triggered by the avalanche, and energy stored in the capacitor will be released along the arc, ablating and ionizing the propellant, and forming plasma. Then, an electromagnetic field is formed between the electrodes due to the self-induced magnetic field (from the current flow) and electrostatic field (between the electrodes) of the discharge arc. Through the Lorentz force, the plasma is accelerated to a high velocity by the electromagnetic field, resulting in a plasma beam (the PPT circuit can be found in the supporting material http://stacks.iop.org/PSST/30/125014/mmedia). All these processes occur in an extremely short period of $\sim$10 μs. Therefore, the transient plasma beam generated by PPTs will exhibit different characteristics when compared with stationary thrusters [28, 29].

A typical discharge current curve from the PPT is shown in figure 2 for an initial discharge voltage of 1800 V (16.2 J). The discharge process exhibited good reproducibility for all cases.

As can be seen in figure 2, the peak discharge current is in the level 20 kA for a single shot. This indicates that a strong induced magnetic field will be generated during the plasma generation and propagation processes. Therefore, the influence of the induced magnetic field on the shockwave formation should also be taken into consideration.

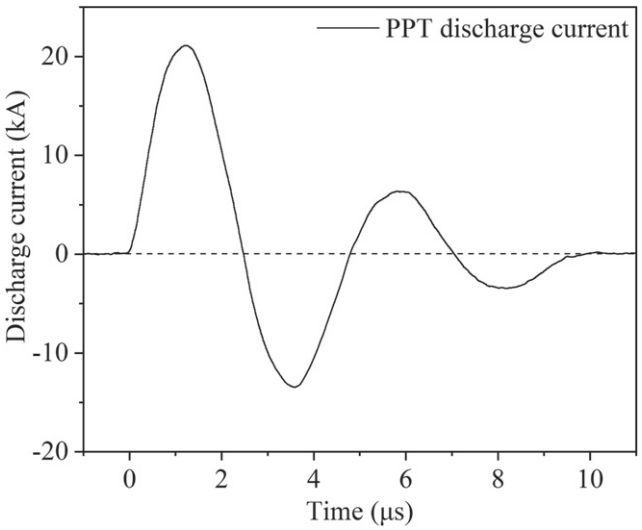

Figure 2. Discharge current waveform of the PPT for an initial discharge voltage of 1800 V (16.2 J). The discharge current exhibits a sinusoidal damping waveform ranging from 0–20 000 A as measured using a Rogowski coil. The discharge waveform has a repeatability error of less than 6%.

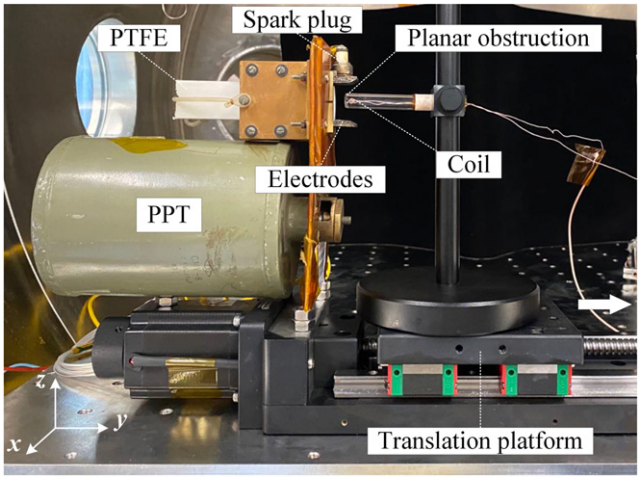

Figure 3. Side-view of the plasma shockwave generation system.

In order to observe shockwave formation from a PPT plasma beam, we set up a planar obstruction probe to generate a plasma shockwave, as shown in figure 3 (the coordinate system for this experiment can also be seen in this figure). The probe is placed in front of the exit plane of the PPT to cause plasma compression of the plasma beam. The probe has a diameter of 10 mm and is assembled on an axial translation platform. To check the formation conditions of shockwaves, different distances from the exit will be studied during the experiments. Inside the probe, two magnetic coils are installed perpendicular to each other, and are used to record the magnetic field. Thus, time-resolved magnetic field variations during shockwave formation and dissipation can be obtained.

The magnetic probe will block the plasma beam emitted by the PPT. A plasma compression process will be observed

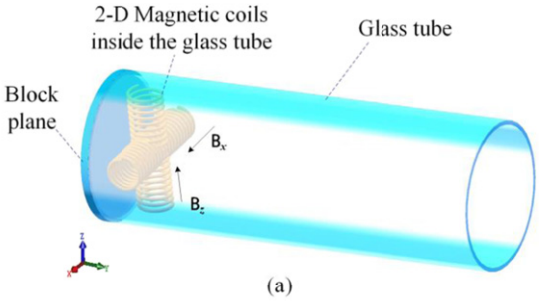

(a) Schematic of the entire planar obstruction probe.

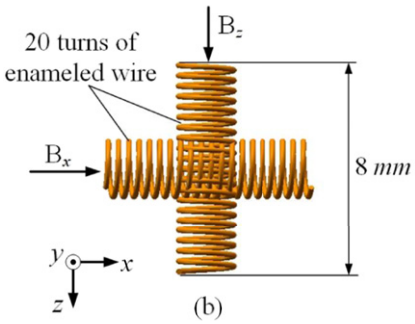

(b) Front view of the inserted 2-D magnetic coils.

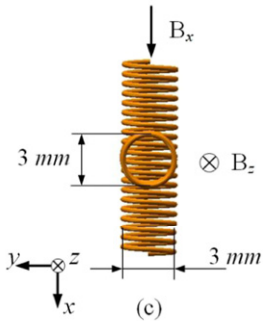

(c) Side view of the inserted 2-D magnetic coils.

Figure 4. Schematic of the coils and the planar obstruction probe.

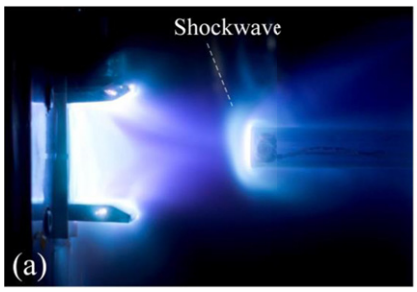

(a) Side view long-exposure image of the plasma shockwave.

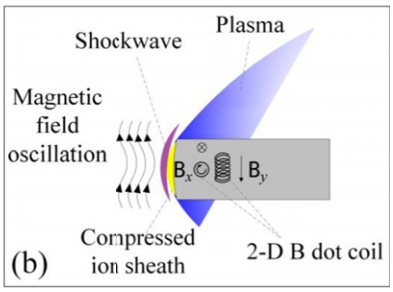

(b) Schematic of the plasma shockwave build-up process.

Figure 5. Plasma shockwave in an in arc-discharge plasma beam. The images were captured with an exposure time (2 s) far greater than the discharge time of ∼10 μs; this presents a composite of the entire discharge process in a single image.

on the probe surface, followed by the buildup and dissipation process of the plasma shockwave. We deliberately increased the diameter of the probe to 10 mm to form a more significant shockwave. Two magnetic coils were inserted into the probe, resulting in an enlarged 2D magnetic probe that can be used to detect the magnetic field in the x-axial and z-axial directions. Figure 4(a) is a schematic of the entire planar obstruction probe. Enlarged details of the 2D magnetic coils located within the outer glass tube shell are shown in figures 4(b) and (c). The shockwave is formed in front of the probe, while the induced local magnetic field can be measured by the coils inside the probe.

The basic fundamentals behind measuring the magnetic field strength follow Faraday's law of electromagnetic induction. The two internal coils are located along the x-axis and z-axis, recording the magnetic flux in two perpendicular directions. The variations in the magnetic field of the discharge plasma will generate an induced voltage on the coils, which is proportional to the intensity of the magnetic field after integration [30]. The coils have 20 turns of enameled wire wound on a plastic core holder with a diameter of 3 mm. Two RC integration circuits are used to integrate the induced voltages on the coils. For calibration, the Biot–Savart law was chosen for ease of calculation of the magnetic flux density along two single axes (calibration curves can be found in the supporting material). Using a translation platform, various measurement distances from the probe to the PPT exit plane (from 1 to 5 cm) can be achieved.

It can be predicted that two physical processes will occur when the plasma is compressed on the probe surface. One

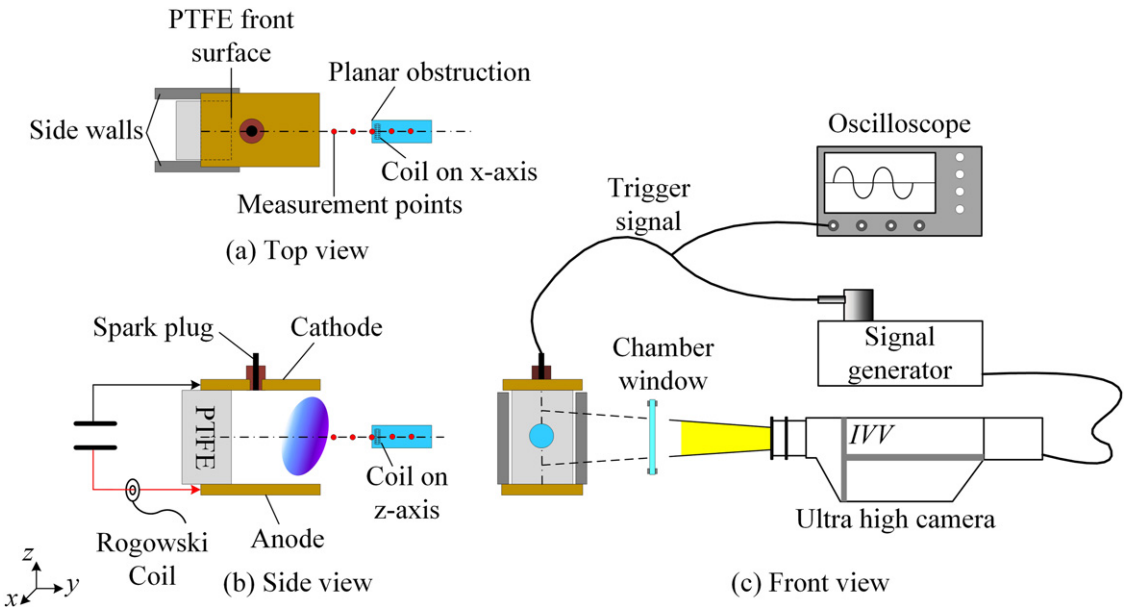

Figure 6. Schematic of the sub-microsecond imaging system. The subject of the experiment is in a vacuum chamber, and there are barriers arranged in front of the PPT to capture the plasma shockwave.

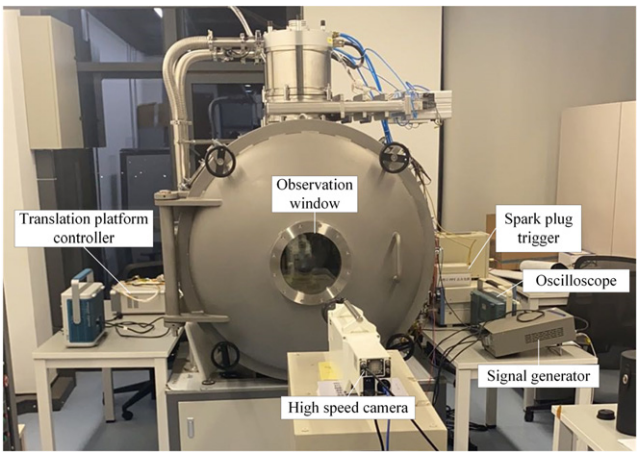

Figure 7. Front-view photograph of the sub-microsecond imaging system.

process is the formation of an ion sheath on the surface (low mass electrons will travel across the shockwave without being influenced), and the other is the oscillation of the surrounding magnetic field caused by the formation of the shockwave. The two internal perpendicularly arranged magnetic coils enable the detection of the magnetic field in two directions. A general broadband emission image of the entire discharge process is shown in figure 5(a) as a visual aid in determining the configuration of the shockwave. A schematic of the plasma shockwave buildup process is shown in figure 5(b). A commercial Nikon D5300 camera was used to capture long-exposure (2 s) images to visualize the plasma shockwaves in this work.

2.2. High-speed imaging system

Considering the extremely short duration of the PPT plasma beams, the shockwave buildup and dissipation process should happen at the sub-microsecond level. Thus, an ultra-high-speed camera was used in this experiment to capture phenomena such as plasma compression, shockwave buildup, plasma expansion, and shockwave dissipation.

In this work, a high-speed imaging system was set up to study the transient build-up and dissipation of the plasma shockwave. This consists of an ultra-high-speed camera (Invisible Vision Ultra UHSi 24), a signal generator (SRS DG535), an oscilloscope (Tektronix DPO3014), a high-voltage probe (Tektronix P5100) to detect the spark plug trigger, a high-voltage probe (Tektronix P5100A) to record the PPT discharge voltage, a Rogowski coil [31], and a control laptop. A schematic of the high-speed imaging system for capturing a PPT discharge is shown in figure 6. A photograph of the high-speed imaging system is shown in figure 7. The high-speed camera is equipped with a Nikon AF-S 70–200 mm f/2.8E lens. This is a high-speed framing camera with a 16 megapixel GigE-linked Charge-Coupled Device (CCD) that can take a series of 12 images at a maximum of 200 million frames per second (fps). Five distances were chosen outside the electrodes along the y-axis. Thus, probe surface distances of 10, 20, 30, 40, and 50 mm from the exit plane were tested in the experiments.

The success of capturing the shockwaves relies on an accurate trigger to both the high-speed camera and the oscilloscope. Through an accurate trigger, we can obtain the PPT's initial discharge time and the period of shockwave formation. For all PPTs, there is an inherent delay between the spark plug firing

and the onset of the discharge [32, 33]. We used the spark plug signal as the initial trigger for the oscilloscope and the signal generator, as shown in figure 8. After the initial trigger, the oscilloscope will be triggered to record the discharge current and voltage of the PPT, while the signal generator outputs a standard Transistor-Transistor Logic (TTL) signal into the high-speed camera to start the shutter. For the signal generator, a variable time delay can be set to coincide with the onset of the PPT discharge or for different periods during shockwave formation. Finally, we can obtain a precise time-correspondence between the PPT discharge and high-speed images.

2.3. Langmuir probe

In this work, we used a cylindrical-type triple Langmuir probe developed in-house [34]. A photo of the triple Langmuir probe can be found in the supplementary material. Three tungsten wires with a diameter of 0.3 mm are used as the three probe electrodes to record the electron density and temperature. Each electrode has a length of 4.5 mm that is exposed to the plasma and a collection surface area of 1.9 mm^2. The three probe electrodes are arranged parallel to the centerline of the thruster, with a distance of 2 mm between each wire, which is much larger than the sheath thickness (∼0.2 mm; thin-sheath regime) around the probe, ensuring that the electrodes do not interfere with each other. We used the triple Langmuir probe to record the local electron density and electron temperature of the arriving plasma. As the Langmuir probe is a fairly mature plasma diagnostic device [35, 36], a review of the probe theory and calculations is located in the supporting material. Five distances were chosen outside the electrodes along the *y*-axis. The distances to the PPT exit plane were 10, 20, 30, 40, and 50 mm. The measurement points and coordinate system of the Langmuir probe are the same as for the planar obstruction probe, with the aim to obtain the plasma parameters at the shockwave positions.

2.4. Vacuum system

All the experiments were conducted in a vacuum environment provided by a multi-functional vacuum system. The system includes a vacuum pumping system and a vacuum chamber. This chamber has an inner diameter of 800 mm and a length of 1500 mm. The vacuum system uses an advanced oil-free, clean molecular pump as the main pump. It can reach an ultimate vacuum degree of 5×10^{-5} Pa (no-load, at a room temperature 20 °C–30 °C). During the experiments with PPT ignition, a vacuum degree of 3×10^{-3} Pa was achieved.

3. Plasma shockwave model

The purpose of this model is to calculate the physical parameters downstream of the shockwave (assuming that the local upstream parameters are known from experimental measurements). The key issue lies with resolving the transition relationship between the upstream and downstream of the shockwave. Thus, the parameters inside the shockwave are neglected in this work. For a discontinuous surface, the MHD equations can be used to obtain the transition relationship on both sides of the shockwave. The balance relations for the upstream and downstream of the shockwave include the continuity equation, momentum equation, and energy equation (solved with the generalized Ohm's law and Maxwell equations). The Maxwell equations are used to resolve the magnetic fields. The generalized Ohm's law is used to describe the relationship between the current and the electric field. Due to the high plasma density and the existence of a magnetic field, the Hall current term cannot be ignored (the electronic thermal pressure term is ignored). The final equations of the shockwave model are as follows:

$$\begin{cases} \dfrac{\partial \rho}{\partial t} = -\nabla \cdot (\rho \vec{u}) & (1) \\ \dfrac{\partial (\rho \vec{u})}{\partial t} = \nabla \cdot \left(-p\vec{\vec{I}} + \vec{\vec{\chi}} + \dfrac{\vec{B}\vec{B}}{\mu_0} - \dfrac{B^2}{2\mu_0}\vec{\vec{I}} - \rho \vec{u}\vec{u} \right) & (2) \\ \dfrac{\partial}{\partial t}\left[\rho\left(\varepsilon + \dfrac{u^2}{2}\right) + \dfrac{B^2}{2\mu_0}\right] = \nabla \cdot \left[(-p\vec{\vec{I}} + \vec{\vec{\chi}}) \cdot \vec{u} - \rho \vec{u}\left(\varepsilon + \dfrac{u^2}{2}\right) - \dfrac{1}{\mu_0}(B^2 \vec{u} - (\vec{B} \cdot \vec{u})\vec{B}) \right. \\ \left. - \dfrac{1}{\sigma_c {\mu_0}^2}\left(\nabla\left(\dfrac{B^2}{2}\right) - (\vec{B} \cdot \nabla)\vec{B}\right) - \dfrac{1}{{\mu_0}^2 ne}((\vec{B} \cdot (\nabla \times \vec{B})\vec{B} - B^2 \nabla \times \vec{B})) - \vec{q} \right] & (3) \\ \nabla \cdot \vec{B} = 0 & (4) \\ \nabla \times \vec{E} = \nabla \times \left(\dfrac{\vec{J}}{\sigma_c} + \dfrac{1}{ne}\vec{J} \times \vec{B} - \vec{u} \times \vec{B} \right) = -\dfrac{\partial \vec{B}}{\partial t} & (5) \\ J = \sigma_c \left[(\vec{E} + \vec{u} \times \vec{B}) - \dfrac{1}{ne}\vec{J} \times \vec{B} \right] & (6) \end{cases}$$

where ρ is the local gas density, t is time, $\vec{u}$ is the plasma velocity, p is the total plasma pressure, $\overleftrightarrow{P} = -p\overleftrightarrow{I} + \overleftrightarrow{\chi}$ is the pressure tensor, $\overleftrightarrow{\chi}$ is the viscosity tensor, $\vec{B}$ is the local magnetic field vector, $\overleftrightarrow{I}$ is the unit tensor, μ_0 is the vacuum permeability, $\varepsilon = \frac{p}{(\gamma-1)\rho}$ is the fluid internal energy, σ_c is the conductivity, $\vec{q} = -\kappa\nabla T$ is the heat flow vector, $\gamma = \frac{c_p}{c_v} = \frac{c_v+R}{c_v}$ is the ratio of the specific heats, $\vec{E}$ is the electric field vector, $\vec{J}$ is the current density vector, n is the plasma density, and e is the elementary electric charge. Equations (1)–(6) are the MHD shockwave equations derived in this work.

To study the plasma shockwave, we can divide the regions into the upstream and downstream with the shockwave discontinuity as the boundary, as shown in figure 9. The upstream plasma parameters including the electron density N_e, electron temperature T_e, and local magnetic field B can be measured using diagnostic equipment. Therefore, we can solve the MHD equations based on the known upstream parameters to obtain the downstream plasma parameters.

One criterion for shockwave formation is the plasma velocity range. When the upstream velocity u_1 is higher than the magnetosonic wave speed while the downstream velocity u_2 is lower than the magnetosonic wave speed, a plasma shockwave can then form. This is shown in equation (7) as follows:

$$u_1 > \sqrt{\frac{B^2}{\rho\mu_0} + \frac{\gamma p}{\rho}} > u_2. \tag{7}$$

In the plasma plume of the PPT, the shockwave is treated as a quasi-steady shockwave in which the buildup time of the shockwave is neglected, that is $\frac{\partial}{\partial t} = 0$. For quasi-steady-state shockwaves, we can use the discontinuity hypothesis (this method can be found in reference [14]) to simplify equations (1)–(5). The shockwave is regarded as a discontinuous plane, and volume integration is performed along the directions perpendicular to the upstream and downstream discontinuity (a detailed derivation process can be found in the supporting material). Thus, from the integration of equations (1)–(5), we can obtain the relationship between the upstream and downstream of the shockwave as follows:

$$\begin{cases}
[(\rho\vec{u})\cdot\hat{n}]\,|_1^2 = 0 & (8)\\
\left[\left(-p\overleftrightarrow{I} + \overleftrightarrow{\chi} + \frac{\vec{B}\vec{B}}{\mu_0} - \frac{B^2}{2\mu_0}\overleftrightarrow{I} - \rho\vec{u}\vec{u}\right)\cdot\hat{n}\right]|_1^2 = 0 & (9)\\
\left[(-p\overleftrightarrow{I} + \overleftrightarrow{\chi})\cdot\vec{u} - \rho\vec{u}\left(\varepsilon + \frac{u^2}{2}\right) - \frac{1}{\mu_0}(B^2\vec{u} - (\vec{B}\cdot\vec{u})\vec{B}) - \frac{1}{\sigma_c\mu_0^{\,2}}\left(\nabla\left(\frac{B^2}{2}\right) - (\vec{B}\cdot\nabla)\vec{B}\right)\right.\\
\left. - \frac{1}{\mu_0^{\,2}ne}((\vec{B}\cdot(\nabla\times\vec{B}))\vec{B} - B^2\nabla\times\vec{B}) - \vec{q}\right]\cdot\hat{n}\,|_1^2 = 0 & (10)\\
B_n\,|_1^2 = 0 & (11)\\
E_t\,|_1^2 = \left(\frac{\vec{J}}{\sigma_c} + \frac{1}{ne}\vec{J}\times\vec{B} - \vec{u}\times\vec{B}\right)_t\,|_1^2 = 0 & (12)
\end{cases}$$

where the subscript '1' represents the upstream terms, the subscript '2' represents the downstream terms, the subscript 't' represents the tangential component along the shockwave discontinuity, the subscript 'n' represents the normal component along the shockwave discontinuity, the symbol '$|_1^2$' represents the difference between the downstream region and the upstream region, and $\hat{n}$ is the direction unit vector perpendicular to the shock discontinuity.

We assume that the plasma flow before and after the shockwave is uniform, and that there is no velocity gradient. Thus, the viscosity term $\overleftrightarrow{\chi}$ is neglected in this work. At the same time, it is assumed that there is no temperature gradient perpendicular to the shockwave plane before and after the shockwave (the temperature gradient only exists inside the shockwave), and so the heat flow term $\vec{q}$ is also neglected. The ions in the PPT plume are considered to be monoatomic ions, with the ratio C^+:F^+ = 1:2, having an average atomic weight M = 16.7. By projecting the transition relation equations (8)–(12) to the x, y, z directions of the shockwave model's coordinate system, we can then obtain eight algebraic equations (the derivation process can be found in the supporting material). Therefore, the parameters downstream of the shockwave can be obtained.

The pressure, density, and magnetic field of the upstream and downstream regions will change due to the shockwave. The ultimate criterion for shockwave formation is as follows:

$$\frac{p_2}{p_1} > 1, \qquad \frac{\rho_2}{\rho_1} > 1, \qquad \frac{B_2}{B_1} > 1. \tag{13}$$

For a time point that satisfies formula (13), a shockwave is determined to exist.

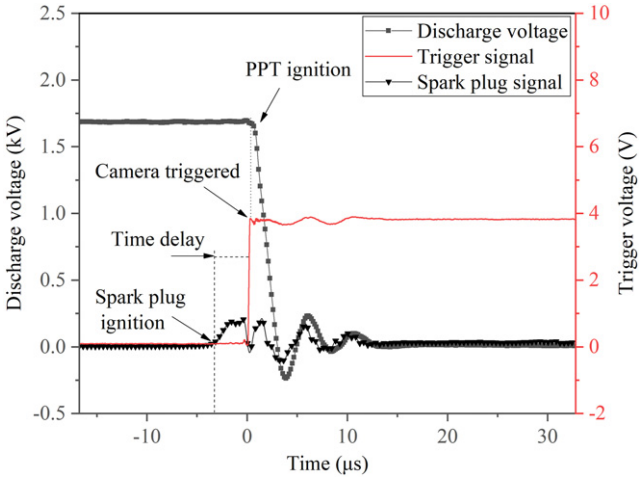

Figure 8. The camera trigger process during PPT ignition.

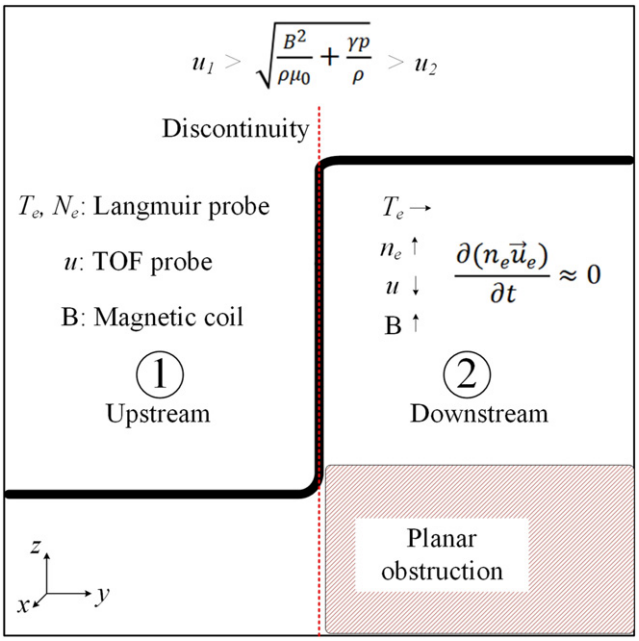

Figure 9. Upstream and downstream relationship for the compressed plasma shockwave.

4. Results and discussion

4.1. Build-up and dissipation process of plasma shock

High-speed images of shockwaves that formed in the PPT plasma beams are shown in figure 10. Locations and geometries of the cathode, anode, planar obstruction probe, and propellant are shown in the first image (0 μs during the initial discharge) using dotted lines. This figure shows the condition with the probe 1 cm from the exit to better illustrate the plasma shockwave. This series of images was taken with an f-number of f/5, a gain of 100, and a frame rate of 2 million fps. During the experiment, the PPT was tested at various initial voltage levels including 1000 V, 1200 V, 1500 V, and 1800 V. In order to best highlight the plasma morphology and the shockwave buildup process, the figures shown correspond to an initial discharge voltage of 1800 V, which resulted in the highest luminosity.

Figure 10 shows the complete period of the shockwave buildup and dissipation process during the PPT's initial main discharge. From this figure, we can clearly see two obvious plasma shockwaves that developed and dissipated during the discharge process. At 1 μs, the plasma reached the planar surface but the compression process has not yet begun. At 1.5 μs, the plasma completely surrounds the probe and a clear bow-shaped discontinuity (1–2 mm in thickness) is formed above the obstruction. In addition, a bright 0.5 mm thick ion sheath is formed on the planar surface (this is assumed to be an ion sheath as the electrons dissipate more easily during the compression process). The shockwave appears to develop in length from 2 μs to 2.5 μs, but the morphology and luminosity tends to be stable. From 3 μs to 3.5 μs, the shockwave also begins to dissipate, even with the presence of plasma around the probe. After 0.5 μs, another new shockwave forms from 4 μs to 4.5 μs. This shockwave is weaker in luminosity and only appeared for a duration of 0.5 μs. After 5 μs, the shockwaves completely dissipated.

From figure 10, we can see that the plasma density is not the only parameter that determines the formation of a shockwave. At 3, 3.5, and 5.5 μs, we can see that even with plasma impacting the probe, a shockwave still did not form. We hypothesize that this is largely due to plasma density and local magnetic field variations. Another point worth noting is that the attack angles for the two shockwaves exhibit a clear difference. The second shockwave that formed at 4 μs to 4.5 μs has a larger attack angle than the first shockwave (from 1.5 μs to 3 μs). This is due to the latter impacting plasma having a lower velocity than the previous plasma generated during the main discharge.

As previously mentioned, a triple Langmuir probe was positioned at the same measurement points as the planar obstruction probe. This can give us a better illustration of plasma density variations at the shockwave formation position. The 1 cm distance from the exit is chosen to study the 1 cm shockwave formation process. The electron density curve at a distance of 1 cm is shown in figure 11 together with the duration of the two shockwaves. The PPT operated at an initial discharge voltage of 1800 V, corresponding to an energy level of 16.2 J.

Due to the quasi-neutrality of the plasma beam generated by the PPT, we will use the peak electron density here as an indicator for the plasma beam density. It is obvious that the two shockwaves were generated from the compression of the same cloud of plasma (the first peak in figure 11), but there was no shockwave formed during the follow-up plasma waves (the 2nd and 3rd electron density peaks). This indicates that while the plasma densities of the first and second peaks are similar, the plasma velocity also plays a key role in the plasma shockwave buildup process (the plasma from the 1st peak has a much higher velocity than that of the 2nd peak). Another point worth noting is that the 1st shockwave dissipated at the peak of the plasma density, while the 2nd shockwave continued to exist until the plasma density reached the lowest value. There was a 1 μs blank period (the dissipation period

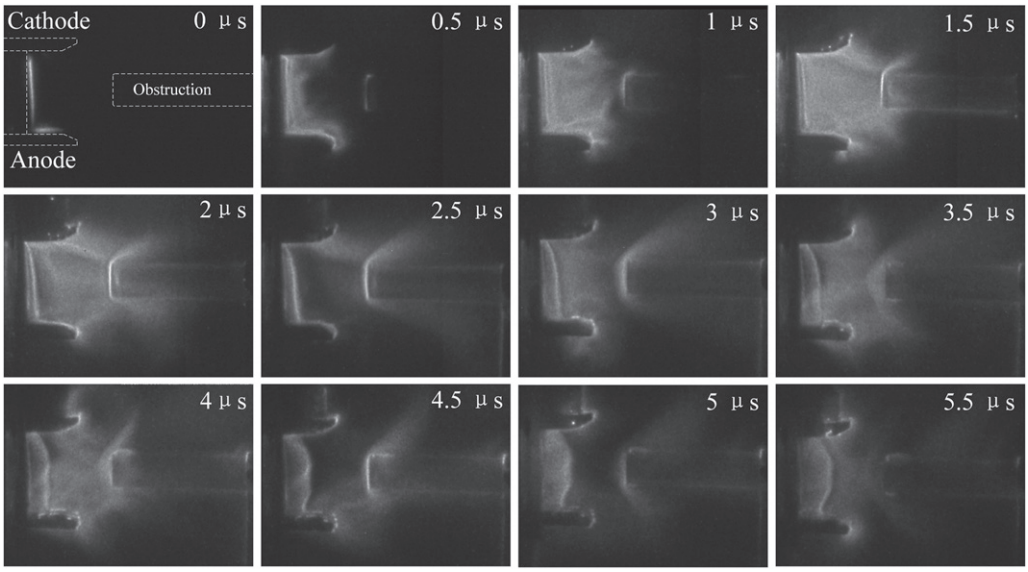

Figure 10. Side-view high-speed images of the plasma shockwave buildup and dissipation process. A frame rate of 2 million fps, $f/5$, an exposure time of 100 ns, and a CCD gain of 100 was used. The PPT's initial discharge voltage was 1800 V (16.2 J).

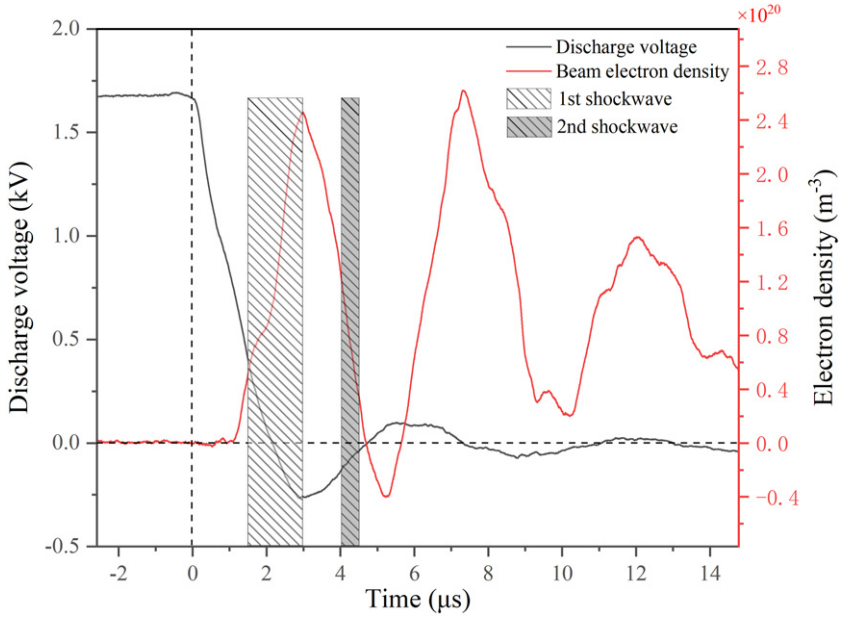

Figure 11. The plotted electron density at a distance of 1 cm from the exit along with the duration of the two shockwaves.

between the two shockwaves) with a high density plasma compressing against the planar surface. This point can also be observed in the high-speed images in figure 10 (at 3.5 μs and 4.5 μs). Excluding the two influencing factors of plasma density and velocity, there are other parameters that also affect the buildup and dissipation of the plasma shockwave. Two possible reasons are considered here for the dissipation process. One reason is because of collisions between the arriving high-density plasma and the 1st plasma shockwave. This will cause wave expansion and dissipation. The other reason is that at 3 μs to 3.5 μs, the local magnetic field may be too strong. Correspondingly, the magnetosonic wave speed will be quite high due to the magnetic field strength, and a plasma shockwave will be unsustainable (as shown in section 3, equation (7)).

The magnetic field was measured using inner coils in the x-axial and z-axial directions. This is aimed at identifying the relationship between the local magnetic field and plasma shockwave formation. Magnetic field curves in the two axial directions can be seen in figure 12. The data is shown for a discharge voltage of 1800 V. As the discharge arc generated between the PPT electrodes is in the z-axial direction, the magnetic field in the x-axial direction will be much stronger than in the other directions.

It is interesting to note that the magnetic field strength in the z-axial direction clearly reflects the buildup of

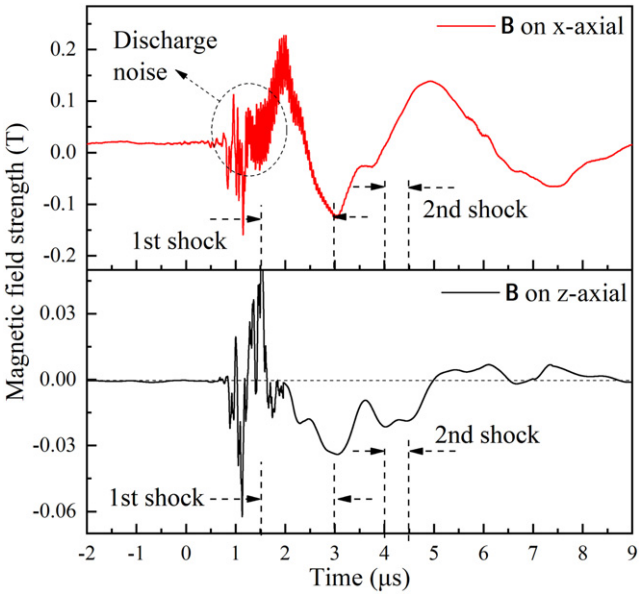

Figure 12. Time-resolved magnetic field strength in the x-axial and z-axial directions. The magnetic field strength B_x is a magnitude higher than B_z. The magnetic waveform for B_z also exhibits two apparent negative peaks, which is mainly due to the disturbance of the shockwaves.

shockwaves in figure 12. The magnetic field exhibits two apparent negative peaks during the two shockwaves. However, the magnetic field in the x-axial direction is not disturbed by the shockwave (the waveform of the measured results is similar to those of the previous results in references [37, 38]). Another point is that the peak magnetic field strength corresponds to the time that the shockwave began to dissipate (for both directions). This suggests that the formation of the plasma shockwave is mainly determined by the local magnetic field strength.

4.2. Plasma shockwave variation with distance

In this section, various distances between the probe and the PPT exit are studied to identify the relationship between the local plasma parameters and shockwave formation. As the distance of the obstruction probe is changed from nearer to further from the exit, the local plasma density, velocity, magnetic field, and shockwave characteristics will all exhibit successive changes. High-speed images for probe distances of 1 cm, 2 cm, and 3 cm are compared in figures 13–15. The PPT was operated at an initial discharge voltage of 1800 V, while the high-speed camera was operated with an f-number of $f/5$ and a gain of 100. The three distances were tested at various frame rates (1, 2, 5, and 10 million fps) and each was repeated at least five times. Here, we selected a discharge voltage of 1800 V and a camera frame rate of 5 million fps to best highlight the shockwave morphology.

Shockwave parameters for probe distances of 1 cm to 5 cm are summarized in table 1. However, we did not observe shockwave formation at distances of 4 cm and 5 cm. The shockwave duration, local magnetic field strength, plasma peak electron density, and attack angle were chosen as key indicators for understanding the buildup and dissipation process of the plasma shockwave.

The maximum repeatability error of Langmuir probe density measurements is less than 10%, much lower than the differences in the peak values [25]. The time resolution for the high-speed imaging results is 0.2 μs, which is a magnitude lower than the shockwave duration. The high-speed images and plasma shockwave parameters in table 1 reveal three aspects regarding the shockwave buildup process: (i) the duration of the shockwave is highly dependent on the local plasma density. As the plasma density decreased with further distances, the duration of the shockwave also tends to decrease with the plasma density; (ii) as the probe distance from the PPT exit increased, the magnetic field intensity in the x-axial direction obviously decreased, while the z-axial magnetic field remained approximately the same in magnitude. This indicates that the compression process of the shockwave is maintained within a stable parameter range during the formation process; (iii) the attack angle of the shockwave gradually increased with distance. It can be observed that the attack angle of the second shockwave is much larger than that of the first shockwave. The physical mechanism behind this is similar to that of shockwaves in fluid mechanics. The second plasma shockwave or the conditions at further distances have a lower Mach number compared to the first shockwave at a distance of 1 cm, and so the shockwave's attack angle is larger.

5. Model verification

Some preliminary calculations for the shockwave model were performed in this work. The shockwave measured at a distance of 1 cm was selected for comparison with the calculation results. The plasma shockwave formation time and duration time were obtained from the shockwave model.

The propellant PTFE is mainly composed of C_2F_4, and thus the neutral species in the arc-discharge plasma beams are mainly composed of C_2, F, and C_2F_4. It can be estimated from the high-speed camera measurements that the neutral C_2 speed is on the level of 1 km s^{-1}, while the C^+ ion velocity is on the level of 20 km s^{-1} [30, 37]. This confirms that the neutral components in the plasma plume are much slower than the ions and cannot reach the probe surface before 5 μs has elapsed (at 1 km s^{-1}, neutrals would have travelled 10 mm in 5 μs, while the probe is located several cm away). The mean free path (MFP) of ion–neutral collisions is 12.6 cm, and the MFP of electron–neutral collisions is 67.4 cm. Therefore, the plasma-gas Knudsen numbers are $\gg 1$. On the other hand, the MFP of ion–ion collisions is 2.61×10^{-6} m, and the MFP of electron–ion collisions is 3.95×10^{-3} m. The plasma collision Knudsen numbers are $\ll 1$ (the Knudsen number calculations can be found in the supporting material). Therefore, it is applicable for us to use a magnetic fluid assumption in our model.

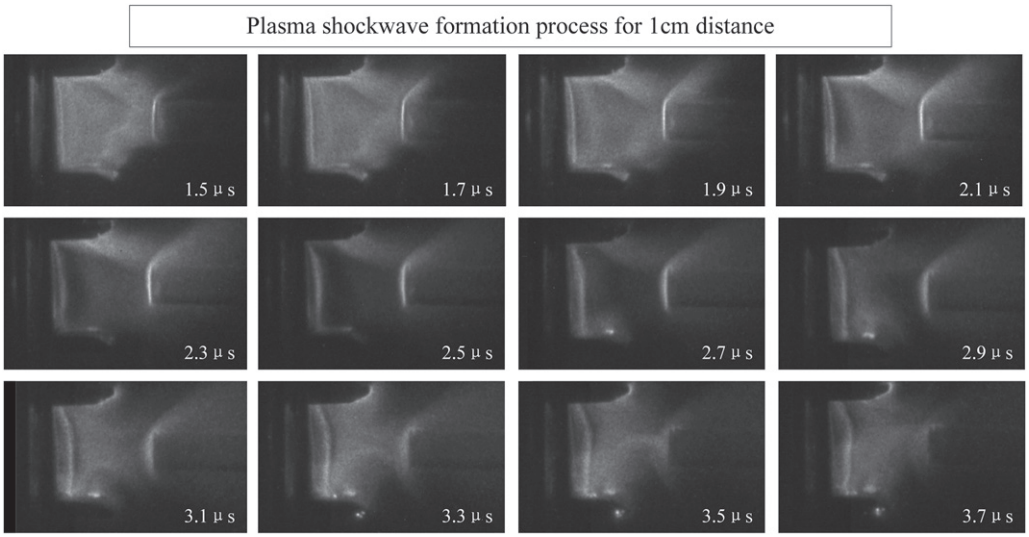

Figure 13. Side-view of the plasma shockwave morphology at a 1 cm distance to the PPT exit. At 1.7 μs, a bow-shaped discontinuity was observed above the probe. At 3.3 μs, the original shockwave has almost disappeared. The shockwave duration was 1.6 μs.

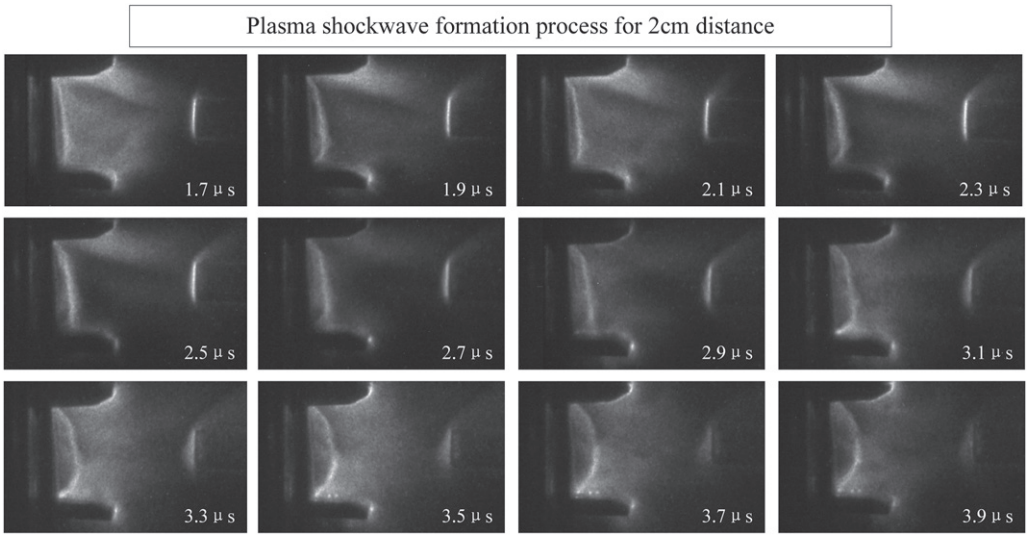

Figure 14. Side-view of the plasma shockwave morphology at a 2 cm distance to the PPT exit. At 2.1 μs, a shockwave was developing. At 3.3 μs, the shockwave has almost dissipated. The shockwave duration was 1.2 μs.

Thus, the shockwave model only take electrons and ions into consideration. The electron–ion collision frequency ν_{ei} [39] is as follows:

$$\upsilon_{ei} = \frac{1}{(4\pi\varepsilon_0)^2}\frac{4\sqrt{2\pi}n_e e^4\ \ln(\Lambda)}{3m_e^{\frac{1}{2}}(kT_e)^{\frac{3}{2}}}. \tag{14}$$

In the calculation process, plasma parameters including the magnetic field B and electron density n_e of the plasma beam were obtained from experimental measurements (shown in table 1): the ion temperature $T_i = 1500$ K, electron temperature $T_e = 6$ eV, $\ln(\Lambda)$ is the Coulomb logarithm, and $\ln(\Lambda) \approx 10$ [40] in the plasma plume of a PPT. The first shockwave attack angle is $\theta_1 = 59^\circ$ and the 2nd shockwave attack angle is $\theta_2 = 62^\circ$. The upstream plasma velocity along the y-axis is $u_p = 30$ km s^{-1} [40]. With the upstream parameters, the downstream pressure and plasma density can be solved from equations (8)–(12). The calculated pressure is the sum of the electron pressure and ion pressure, with electrons being the main contributor. The time-varying parameters for the pressure, magnetic field, and plasma density downstream of the shockwave can be seen in figure 16.

Time periods where equation (13) is satisfied are determined to be times where a shockwave exists. According to the plasma shockwave model, we can obtain the relationship between the upstream and downstream of the shockwave. The relationship between the upstream and downstream pressure,

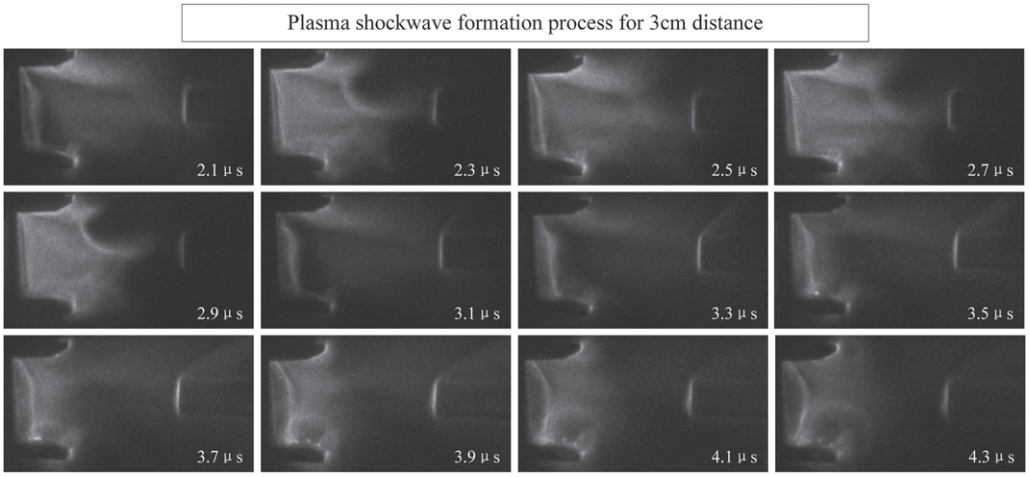

Figure 15. Side-view of the plasma shockwave morphology at a 3 cm distance to the PPT exit. At 3.1 μs, a shockwave was developing. At 3.7 μs, the shockwave has almost dissipated. The shockwave duration was 0.6 μs.

Table 1. Local plasma shockwave parameters for five probe distances[a].

		B (T)				
D (mm)	t_d (μs)	x-axial	z-axial	n_e (m^{-3})	Attack angle (°)	
10	1.6	0.21	0.034	2.6×10^{20}	59	62
20	1.2	0.11	0.033	1.9×10^{20}	62	N/A*
30	0.6	0.098	0.027	1.4×10^{20}	65	N/A*
40	0	0.006*	N/A*	1.2×10^{20}	N/A*	N/A*
50	0	N/A*	N/A*	1.0×10^{20}	N/A*	N/A*

[a]Note: D, distance to PPT exit; t_d, shockwave duration time; B, magnetic field; n_e, peak electron density measured by triple Langmuir probe, and is treated as the electron density upstream of the shockwave; attack angle, the angle between the shockwave discontinuity and the y-axis; θ_1, 1st shockwave attack angle; θ_2, 2nd shockwave attack angle; N/A, not available (because the magnetic field was too weak to be recorded); *, shockwave did not form.

density, and magnetic field are summarized as dimensionless ratios in figure 17.

Based on the calculation results of the upstream and downstream parameters, durations with a ratio greater than 1 are determined to exhibit shockwave formation. Therefore, the shockwave buildup times and duration can be obtained from the model. The shockwave buildup and duration periods are shown in figure 18. The corresponding magnetic field curves in the x-axial direction is shown in black lines to better indicate the influence of the magnetic field on the shockwave buildup process.

It is clear at first glance that the model also predicts two shockwaves and the dissipation process. The calculation results fall within the experimental observation time period. The number of shockwaves generated and the results of the dissipation time period are in good agreement between the model and experiments. This explains from a theoretical point of view that the magnetic field, density, and plasma velocity in the magnetic fluid together affect the buildup process of the shockwave. The fluctuation in the magnetic field causes variations in the magnetosonic wave speed. Therefore, we observed that a second shockwave formed and passed through the same plasma medium.

However, it is apparent that the calculation results are not fully accurate, and that the buildup time and duration did not match the experimental results. This is largely due to two problems that have not yet been solved at the current stage: (1) the plasma compression process is still unknown. The density measured by the Langmuir probe (aspect ratio > 10) does not fully reflect the plasma compression process at the planar obstruction probe. An increase in plasma density will cause the magneto-acoustic velocity to decrease, which will make the shockwave last longer. Therefore, the observed duration of the first shock in the experiment is greater than that of the theoretically calculated duration; (2) judging shockwave formation from high-speed images is subjective. The difference between the shockwave judgment method in experiments and in theoretical calculations may also cause a deviation in the comparisons.

This plasma shockwave model serves to provide a more general understanding of the shockwave buildup and dissipation process in PPTs. In the future, to develop this model into

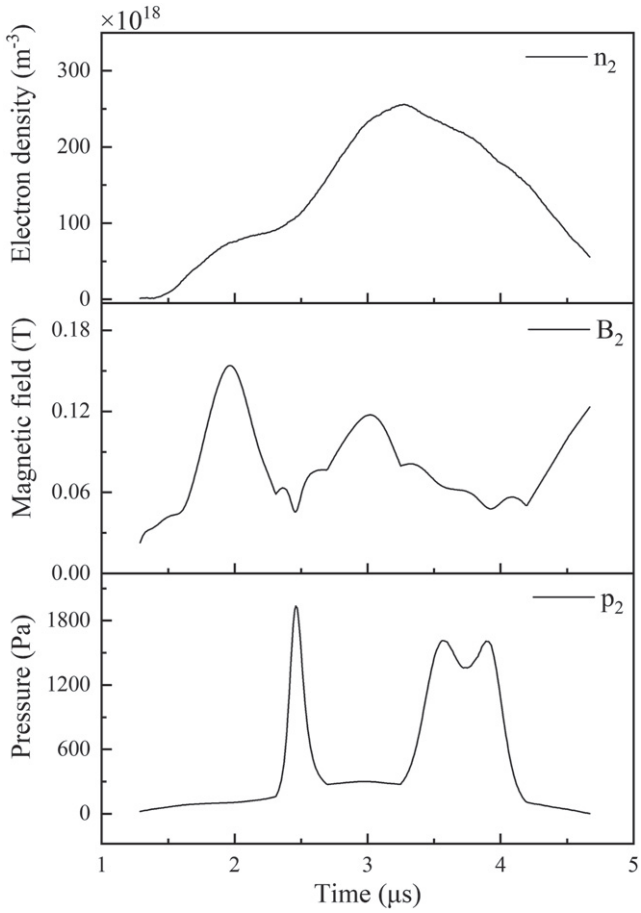

Figure 16. Calculated parameters for the pressure, magnetic field, and plasma density downstream of the shockwave.

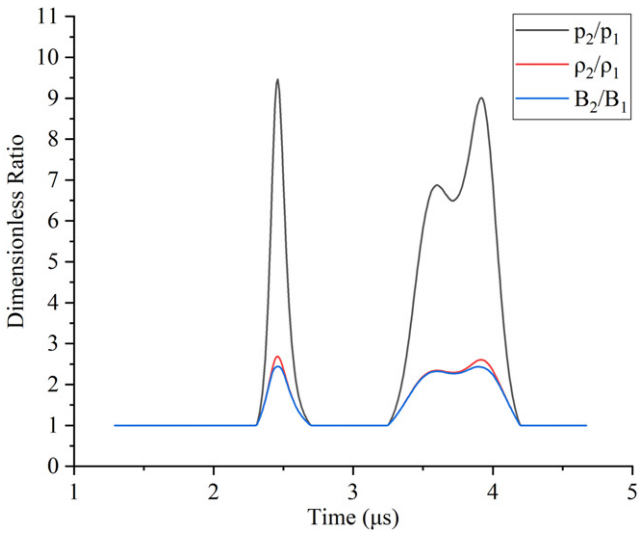

Figure 17. The relationship between upstream and downstream pressure, density, and magnetic field.

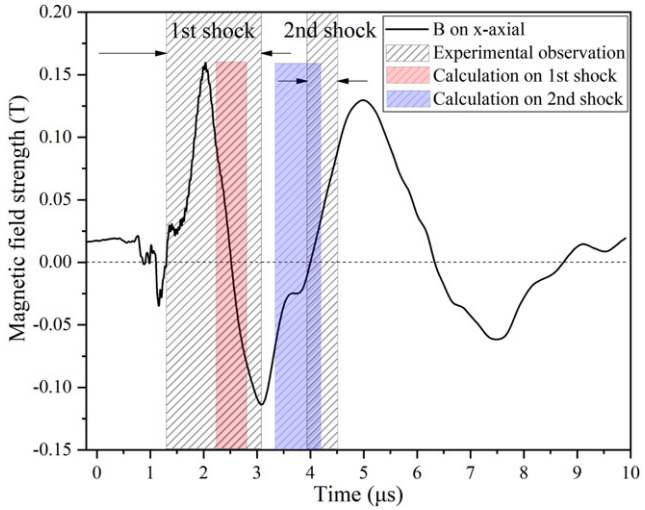

Figure 18. Buildup and duration period for the plasma shockwave.

a more accurate predictor, more accurate input plasma parameters should be obtained. In addition, we also plan to take the viscous term, elementary reaction collision term, and neutral gas collision term into consideration to obtain a more accurate calculation.

6. Conclusion

In the present work, a detailed time-resolved study of a transient plasma shockwave produced from a planar obstruction probe compressing the plasma beam from a PPT has been performed through the use of an ultra-high-speed imaging technique. The buildup and dissipation process of the shockwave was recorded using a high-speed imaging system. The 2D local magnetic fields at the shockwave formation plane were measured using two magnetic coils positioned inside the planar obstruction. The corresponding local plasma density was obtained using a Langmuir probe in the experiment. A magnetic fluid model was introduced to assist in sorting out the key indicating parameters to obtain a fundamental understanding of the plasma shockwave buildup and dissipation mechanism.

This research brings new insights to aid in understanding the shockwave buildup mechanism in low temperature plasma beams. Apparent plasma shockwaves were observed to form during the PPT discharge period. The plasma beam was exhausted towards the planar obstruction, and after a 0.5–1 μs period of compression, a 1–2 mm thick plasma shockwave was formed surrounding the planar obstruction and a clear bow-shaped discontinuity was observed above the obstruction. When the distance to the PPT exit was increased from 1 cm to 5 cm, the duration of the shockwaves decreased from 2.0 μs to 0.8 μs, and finally failed to develop. The attack angle of the shockwave increased from 59° to 65° as the distance increased from 1 cm to 3 cm, which follows the pattern in fluid mechanics. The corresponding time-resolved plasma

density and magnetic field were also recorded. It is interesting to note that two shockwaves formed in the first cloud of plasma. Magnetic field strength oscillation occurs in the weaker direction (z-axial), and the peak magnetic field strength corresponds to when the shockwave began to dissipate. This indicates that the local magnetic field strength affects the formation of plasma shockwaves by affecting the speed of magnetosonic waves. The magnetic fluid model introduced in this work explains the three key factors (plasma density, magnetic field, and velocity) behind shockwave formation from a theoretical point of view. The local magnetic field and plasma density profiles were used as input to verify the magnetic fluid model. The results (shockwave formation and duration time) from the theoretical model are in good agreement with the experimental results.

We observed the complete plasma shockwave formation and dissipation process both from the qualitative shockwave morphology and from quantitative plasma parameter measurements. Although this paper demonstrates the phenomenon that plasma shockwaves can be formed between electric thrusters and an obstruction, further in-depth studies with other plasma sources operating with different mechanisms are still necessary. One of the main directions for future work is to identify the disturbances in the shockwave and changes in plasma parameters. These are related to the influence on diagnostic accuracy and the selection of contact probe measurement points. Additionally, further studies on the plasma shockwave model are also planned in the future. The analysis in this work can also be applied to other plasma beams in the scope of magnetic fluids, and is not limited to the EP area. The experiments and theoretical model can be used as an example in applying the process in future plasma shockwave analyses. A more general model is planned for determining the buildup conditions for plasma shockwaves in low-temperature plasmas. These studies will possibly aid in a more advanced understanding of plasma shockwaves and plasma diagnostic technology devoted to the overall plasma physics community.

Acknowledgments

The authors would thank Professor Xilong Yu at Institute of Mechanics, Chinese Academy of Sciences for his great help in our high-speed camera experiments. This work was partly supported by the CSC-DAAD fellowship (No. 57531629). Part of the experimental work are supported by the Defense Industrial Technology Development Program JCKY2020601C026.

Data availability statement

All data that support the findings of this study are included within the article (and any supplementary files).

ORCID iDs

Zhe Zhang https://orcid.org/0000-0002-3691-0677
Zun Zhang https://orcid.org/0000-0002-1981-8852
Xin Lin https://orcid.org/0000-0002-6230-438X
William Yeong Liang Ling https://orcid.org/0000-0003-4181-1291
Haibin Tang https://orcid.org/0000-0002-9190-7323
Georg Herdrich https://orcid.org/0000-0002-3957-762X

References

[1] Levchenko I, Xu S, Wu Y-L and Bazaka K 2020 *Nat. Astron.* **4** 1012–4
[2] Levchenko I, Xu S, Mazouffre S, Lev D, Pedrini D, Goebel D, Garrigues L, Taccogna F and Bazaka K 2020 *Phys. Plasmas* **27** 020601
[3] Boeuf J-P 2017 *J. Appl. Phys.* **121** 011101
[4] Lieberman M A and Velikovich A L 1986 *Physics of Shock Waves in Gases and Plasmas* (*Springer Series in Electronics and Photonics*) (Berlin: Springer)
[5] Devaux D, Fabbro R, Tollier L and Bartnicki E 1993 *J. Appl. Phys.* **74** 2268
[6] Müller R A, Pagan A S, Upadhyay P P and Herdrich G 2019 *J. Thermophys. Heat Transfer* **33** 1018–25
[7] Pidan S, Auweter-Kurtz M, Herdrich G *et al* 2004 Determination of recombination coefficients and spectral emissivity of thermal protection materials *37th AIAA Thermophysics Conf., AIAA-2004-2274* (Portland, Oregon)
[8] Yordanov D, Lishev S and Shivarova A 2016 *J. Appl. Phys.* **119** 183302
[9] Wang B, Yang W, Tang H, Li Z, Kitaeva A, Chen Z, Cao J, Herdrich G and Zhang K 2018 *Meas. Sci. Technol.* **29** 075302
[10] Lindl J D, McCrory R L and Campbell E M 1992 *Phys. Today* **45** 32–40
[11] Lee M-J and Jung Y-D 2018 *Plasma Sources Sci. Technol.* **27** 025010
[12] Jorns B A, Mikellides I G and Goebel D M 2014 *Phys. Rev.* E **90** 063106
[13] Horie Y 2007 *Shock Wave Science and Technology Reference Library* (Berlin: Springer)
[14] Boyd T J, Boyd T J M and Sanderson J J 2003 *The Physics of Plasmas* (Cambridge: Cambridge University Press) ch 5
[15] Sorasio G, Marti M, Fonseca R and Silva L O 2006 *Phys. Rev. Lett.* **96** 045005
[16] Leroy M M, Winske D, Goodrich C C, Wu C S and Papadopoulos K 1982 *J. Geophys. Res.* **87** 5081–94
[17] Balogh A and Treumann R A 2013 *Physics of Collisionless Shocks: Space Plasma Shock Waves* (Berlin: Springer)
[18] Fiúza F *et al* 2012 *Phys. Rev. Lett.* **109** 215001
[19] Silva L O, Marti M, Davies J R, Fonseca R A, Ren C, Tsung F S and Mori W B 2004 *Phys. Rev. Lett.* **92** 015002
[20] Mazouffre S 2016 *Plasma Sources Sci. Technol.* **25** 033002
[21] Levchenko I, Baranov O, Fang J, Cherkun O, Xu S and Bazaka K 2021 *Aerosp. Sci. Technol.* **108** 106343
[22] Zhang Z, Tang H, Zhang Z, Wang J and Cao S 2016 *Rev. Sci. Instrum.* **87** 123510
[23] Schönherr T, Komurasaki K, Hörner S, Arakawa Y and Herdrich G 2014 *IEEE Trans. Plasma Sci.* **43** 226–33
[24] Zhang Z, Ling W Y L, Tang H, Cao J, Liu X and Wang N 2019 *Rev. Mod. Plasma Phys.* **3** 5
[25] Zhang Z, Ren J, Tang H, Ling W Y L and York T M 2017 *Plasma Sources Sci. Technol.* **27** 015004
[26] Keidar M, Boyd I D, Antonsen E L, Burton R and Spanjers G G 2006 *J. Propul. Power* **22** 48–55
[27] Macheret S O, Ionikh Y Z, Chernysheva N V, Yalin A P, Martinelli L and Miles R B 2001 *Phys. Fluids* **13** 2693–705

[28] Taccogna F and Garrigues L 2019 *Rev. Mod. Plasma Phys.* **3** 12
[29] Zhang Z, Zhang Z, Xu S, Ling W Y L, Ren J and Tang H 2021 *Aerosp. Sci. Technol.* **110** 106480
[30] Zhang Z, Ling W Y L, Ren J, Tang H, Cao J, Lin X and York T M 2019 *Plasma Sources Sci. Technol.* **28** 025008
[31] Zhang Z, Ren J, Tang H, Ling W Y L, York T M and Cao J 2018 *J. Phys. D: Appl. Phys.* **51** 395201
[32] Kamezaki H, Yano K, Kato H and Horisawa H 2018 Effect of discharge pulse delays on characteristics of a short-pulse Laser-assisted pulsed plasma thruster *51st AIAA/SAE/ASEE Joint Propulsion Conf., AIAA Propulsion and Energy Forum, AIAA 2018-4590* (Orlando)
[33] Huang T, Wu Z, Liu X, Xie K, Wang N and Cheng Y 2015 *Phys. Plasmas* **22** 103511
[34] Zhang Z, Zhang Z, Ling W Y L, Han X, Zhou J, Tang H and Cao J 2020 *J. Phys. D: Appl. Phys.* **53** 475201
[35] Chen S L and Sekiguchi T 1965 *J. Appl. Phys.* **36** 2363–75
[36] Eckman R, Byrne L, Gatsonis N A and Pencil E J 2001 *J. Propul. Power* **17** 762–71
[37] Koizumi H, Noji R, Komurasaki K and Arakawa Y 2007 *Phys. Plasmas* **14** 033506
[38] Lau M and Herdrich G 2014 *Vacuum* **110** 165–71
[39] Goldston R J 2020 *Introduction to Plasma Physics* (Boca Raton, FL: CRC Press) ch 11
[40] Ling W Y L, Zhang Z, Tang H, Liu X and Wang N 2018 *Plasma Sources Sci. Technol.* **27** 104002